Cavitation 91 Symposium, 1st ASME-JSME Fluids Engineering Conference , 23-27 June 1991, Portland (Oregon)

NUMERICAL COMPUTATION OF A LEADING EDGE CAVITY

Ph. Dupont† and F. Avellan
Institut de Machines Hydrauliques et de Mécanique des Fluides
EPFL- Swiss Federal Institute of Technology, Lausanne,
Switzerland

ABSTRACT

Recent work using the IMHEF cavitation tunnel has shown Reynolds effects on the development of a partial leading edge cavity over a NACA 009 profile. These effects, beginning from a Reynolds number of $2 \cdot 10^6$, were followed up to values of $4 \cdot 10^6$. To understand the physics involved, numerous experiments such as pressure, velocity, cavity shape and force measurements were performed. Based on these results, boundary conditions, especially over the cavity, were established and introduced into a Navier-Stokes code in order to calculate the steady situation. The cavity shape was calculated by an iterative process whose initial conditions were given by an indirect potential code. A comparison of these calculations with the experimental results for a Reynolds number of $2 \cdot 10^6$ shows that the former are very accurate. Some differences between velocity measurements and their calculation lead to the identification, in the measurements, of the signature of travelling vorticity structures generated at the leading edge of the foil and convected by the mean flow.

NOMENCLATURE

σ	Cavitation number	$\frac{p_\infty - p_v}{\frac{1}{2}\rho U_\infty^2}$	[-]
C_p	Pressure coefficient	$\frac{p - p_\infty}{\frac{1}{2}\rho U_\infty^2}$	[-]
Re	Reynolds number	$\frac{U \cdot L}{\nu}$	[-]
C_x	Drag coefficient	$\frac{F_x}{S\frac{1}{2}\rho U_\infty^2}$	[-]
C_z	Lift coefficient	$\frac{F_z}{S\frac{1}{2}\rho U_\infty^2}$	[-]
BV	Influence factor		[-]
F_x	Drag force		[N]
F_z	Lift force		[N]
L	Hydrofoil chord length		[m]
P_∞	Upstream static pressure (reference)		[Pa]
P_v	Vapour pressure		[Pa]
S	Hydrofoil area		[m^2]
U_∞	Upstream velocity (reference)		[$m \cdot s^{-1}$]
k	Turbulence kinetic energy per mass unit		[$m^2 \cdot s^{-2}$]
x_c	Cavity length		[m]
x, y	Space coordinates		[m]
ε	Turbulence viscous dissipation per mass unit		[$m^2 \cdot s^{-3}$]
ζ_j	Singularity of complex source type		[-]
κ	Penalty factor		[-]
ν	Cinematic viscosity		[$m^2 \cdot s^{-1}$]

† Now at Ecole Navale de Brest, 29240 Brest-Naval, France.

INTRODUCTION

The prediction of cavitation erosion is one of the major problems involved in hydraulic machine design. This is mainly due to the increase in their specific power. For cost reasons, hydraulic machines tend to become smaller for the same power generation. This problem is more and more topical due to the large number of old units being rehabilitated, where the aim is to increase the power within the same overall geometry. For this reason, prediction must be even more accurate.

Cavitation erosion prediction has two aspects : the localisation of damage and its rate. The maximum damage area having been found to be strongly correlated to the closure of a partial cavitation sheet, a lot of work has been done in order to calculate the length of this main leading edge cavity. The methods used to do these calculations are as numerous as they are different. Potentiel calculations using the conformal mapping, indirect or inverse singularities methods [1], experimental based approches as the equivalent lift method [2], and Euler codes have been used with varying success. Our experience with potential calculation [3] has shown us to be very sensitive to the cavity closure model used and to lead to an underestimation of the main cavity length. Moreover, our experimental results [4] revealed a strong Reynolds effect on the leading edge cavity development, which seems to indicate that turbulent viscosity effects must be taken into account in accurate cavity length prediction.

Recently, unsteady calculations of a leading edge cavity have been done with Euler [5] or with Navier-Stokes [6] codes, including a void fraction model, trying to determine the production rate of the travelling erosive cavities, mainly vortices. These methods are very

The above obviously proves the need for a very good knowledge of the physics involved in leading edge cavity development in order to modelise it. With this aim, numerous experiments have been carried out in the High Speed Cavitation Tunnel on a NACA 009 hydrofoil. These experiments were : main cavity length and shape measurements by image processing, mean static pressure measurements over the surface of the hydrofoil, 2–D LDA measurements over, and in the wake, of the main cavity, erosion intensity and localisation measurement using electrochemical detectors and hydrodynamic force measurement using a five-component balance.

Based on the analysis of these measurements, boundary conditions were estimated, especially over the main cavity, and used to perform calculations with a commercial Reynolds Averaged Navier-Stokes code [7] in a cavitating steady situation. The cavity shape was established using an iterative process in order to correct an initial shape given by the potential solution.

EXPERIMENTAL SET-UP

The IMHEF high speed cavitation tunnel

All the experimental set-ups described in the following and used to validate the computational results are part of the IMHEF High Speed Cavitation Tunnel equipment. This tunnel [10] has a square test section of 150mmx150mm, 750 mm in length, in which velocities up to 50 m/s can be reached. The hydrofoil used for the present study was a symmetrical NACA 009 profile with a maximum thickness of 10 mm at 45 % of the chord length. For mechanical and instrumentation reasons, it was truncated at 90% of the chord, and the resulting chord length was 100 mm. A revolving bed-plate flange provided a rigid mounting-base for the blade, with the possibility of varying the angle of incidence.

Pressure measurements

The mean wall pressure distribution over the hydrofoil is measured by a water pressure line scanning system. These lines are connected to 19 pressure taps, 0.5 mm in diameter, and distributed streamwise over the blade. A very sensitive pressure transducer is isolated from the water by silicone oil. An automatic drain procedure is followed as long as necessary, in order to remove all the undesirable bubbles in every pressure line during cavitation tests.

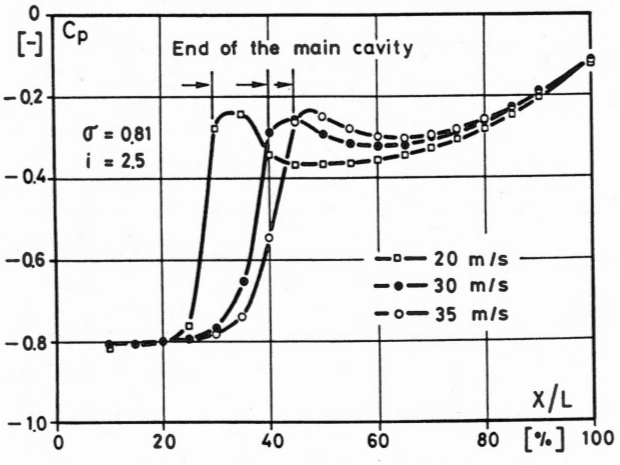

Figure 1 Experimental pressure coefficient distribution for a sigma value of 0.81 at different upstream velocities.

All the pressure acquisitions and the scanning system displacements are remote controlled by a computer. Each pressure measurement corresponds to a mean over half a second, and 30 measurements are used to calculate the average value and a standard deviation for each station.

Measurements are done for different upstream velocities and different sigma values for an angle of incidence of 2.5 degrees. A strong Reynolds effect is revealed by these measurements from values of $2 \cdot 10^6$ up to $3.5 \cdot 10^6$. As an example, the pressure coefficient distribution at different upstream velocities is shown in Figure 1 for a sigma value of 0.81.

Comparing these pressure coefficient distributions with simultaneous top views, it is found that the maximum pressure recovery point corresponds to the average end of the cavity. The evolution of the mean relative cavity length x_c/L with the upstream velocity U_∞ is thus established for different sigma values (see Figure 2). The accuracy of these curves is limited by the pressure tap distribution, allowing the maximum recovery pressure point to be determined within ± 2.5 mm.

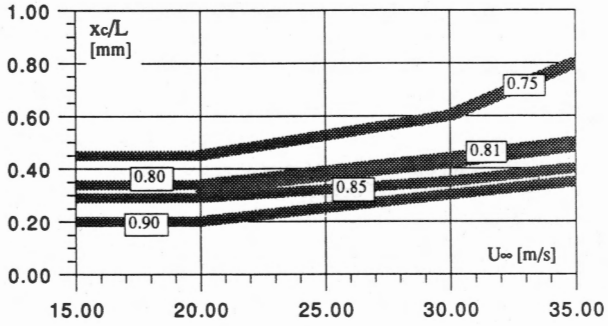

Figure 2 Evolution of the mean relative cavity length with the upstream velocity for a NACA 009 profile at an angle of 2.5 degrees.

Velocity measurements

The two components of the flow velocity in the test section are given by a 2-D Laser Doppler Anemometer with a remote mechanical system for positioning the measuring volume. The accuracy of this traversing system is 0.01 mm on each axis. All the mechanical elements and the optics are mounted on a granite bench supported by four pneumatic shock absorbers. The optical arrangement of the LDA is that of a backward scattering system using 3 beams of two colors. The Doppler bursts of the two frequency shifted signals are processed by two counters. An original data processing software has been developed in order to estimate the statistical values of interest, such as the two components of the mean velocity, the Reynolds stress tensor and the power density spectrum of the velocity fluctuations. Statistical estimates are weighted by the residence time of the particle in the measuring volume. No special tracers are used during the experiments, so they are mainly micro-bubbles.

The flow field investigation is carried out over the hydrofoil suction side only for an upstream velocity of 20 m/s and an incidence angle of 2.5 degrees. The mean velocity components, Vx,Vy and the mean Reynolds stress tensor components $\overline{v'^2_x}$, $\overline{v'^2_y}$ and $\overline{u'v'}$ are measured along 12 transverse profiles, 3 of them above the main cavity, 5 in the cavity closure region and 4 in the pressure recovery part of the flow. Each transverse profile is made through a set of about a hundred measuring points whose spacing depends on the velocity gradient. The mean quantities of interest for each measuring

second image is recorded, in the cavitating situation. The exposure time of the camera is a few milliseconds and the lighting of the laser sheet is continuous, so the resulting image is the mean position of the fluctuating cavity. An example of both recorded images is given in Figure 5, for an angle of incidence of 2.5 degrees, an upstream velocity of 20 m/s and a sigma value of 0.81.

The images thus recorded are treated using an image processing software in order to determine the coordinates of the reflected light outlines. In practice, the outlines are defined as the lightest pixel on a vertical line of the image. In order to simplify the numerical treatment of these images, the assumption is made that a linearization of the transformation equations from the image to the real plane is possible, the angle of incidence of the camera and the optical aberrations being small. We thus applied a usual least squares method to characteristic hydrofoil outline points, such as leading edge, trailing edge and maximum thickness, in order to determine the coefficients of the linear geometric transformation given by :

$$x' = A_1x + B_1y + C_1 + \varepsilon_x$$
$$y' = A_2x + B_2y + C_2 + \varepsilon_y \qquad (1)$$

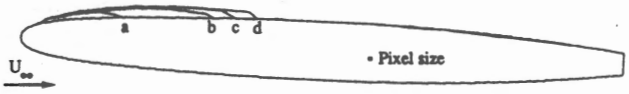

Figure 6 Cavity shapes corresponding to different sigma values for a NACA 009 hydrofoil with an angle of incidence of 2.5 degrees and an upstream velocity of 20 m/s. σ = (a) 0.92; (b) 0.81; (c) 0.77 and (d) 0.75.

This geometric transformation is then used to obtain the actual cavity shape. Some results of this treatement are given in Figure 6 for different sigma values for a NACA 009 profile with an angle of incidence of 2.5 degrees and an upstream velocity of 20 m/s. The theoretical shape of the hydrofoil and its image after processing are superimposed on the cavity sahpes. The accuracy of the measurement is limited by the definition of the image. The latter is formed by 512x512 elementary points (pixels), and the resulting dimensions given by the processing are accurate to ± 0.2 mm.

Hydrodynamic forces measurement

The evolution of the hydrodynamic forces with variation of cavitation number was followed. For this, the hydrofoil was mounted on a five-axes balance resting on the revolving support cylinder. This balance consists of an H-shaped cross-section cantilever beam onto which five complete strain-gauge bridges are cemented.

These measurements are done by a programmable amplifier with $2.5 \cdot 10^{-3}$ % full-scale accuracy, which scans sequentially the five measuring points and transmits the data to the computer. The overall absolute accuracies of the balance given by calibration were within a range of ± 1.5 N for the lift and ± 0.5 N for the drag. This corresponds, in our case, to an accuracy of ± 2.5 % for the lift coefficient C_z and of ± 1.5 % for the drag coeffiecient C_x, mainly due to the accuracy of the upstream velocity measurement.

In some cases, the occurrence of cavitation has been shown to reduce the drag coefficient of a lifting hydrofoil [11]. For our NACA 009 profile, we did not find any significant decrease in the drag forces with the inception of cavitation. Both drag and lift forces increase monotonously when the cavitation number decreases, their ratio being unchanged. This ratio C_z/C_x was equal to 15.3 for an angle of incidence of 2.5 degrees and a Reynolds number based on the chord length of $2 \cdot 10^6$.

CALCULATIONS

Method description

To include the effects of turbulence in our calculations, we injected the geometric solution of a potential code for a given cavity length into a Navier-Stokes code. Using an iterative process, we then reshaped the cavity in order to obtain a constant pressure distribution over it. The modification of the cavity slope, for a given abscissa, was calculated as a function of the pressure distribution slope given by the previous calculation step i :

$$\Delta y_{i+1} = \Delta y_i + C \cdot \Delta Cp_i \qquad (2)$$

Potential code

The potential code used for the initial cavity shape calculation is based on an indirect panel method with a linear distribution of sources on them in the complexe plane [3]. This complex representation in fact correspond to the addition of eddy and source singularities in the real plane. The support points of the panels are disposed slightly inside the profile outline with a sinusoïdal distribution from the leading edge to the trailing edge to increase the number of panels in the strong velocity gradient areas. The velocity control points are located on a line normal to the center of these panels on the profile outline. The upper and lower test section walls are taken into account for the calculation. A correction factor of the upstream velocity is included to take into account the blockage effect due to the development of the boundary layers on the test section walls as well as on the profile.

The velocity components at any control point (x_i, y_i) can be written as a linear composition given by the sum of the contributions of each j panel i.e. :

$$Vx_i = U_\infty \cos \alpha_\infty + \sum_j BVx_{ij} \zeta_j$$
$$Vy_i = U_\infty \sin \alpha_\infty + \sum_j BVy_{ij} \zeta_j \qquad (3)$$

where BVx_{ij} and BVy_{ij} are the influence factors of the j^{th} panel in the i^{th} control point. These influence factors are analytically deduced, taking into account the linear source distribution over the j^{th} panel whose extrema values are ζ_j and ζ_{j+1}.

The cavitation-free conditions are calculated with a normal velocity component v_n equal to zero everywhere on the profile and on the test section walls. A Kutta condition is given at the trailing edge of the profile, expressed by a zero source value at this point. For the truncated trailing edge, the panels before the corners have been slightly expanded in the profile slope direction in order to impose a velocity parallel to this direction at these points. All these boundary conditions can be expressed as a matrix system where the unknowns are the source values :

$$A_{ij} \cdot \zeta_j = B_i \qquad (4)$$

The A_{ij} matrix term consists of an influence factor composition given by the velocity components or profile slope constraints. The B_i matrix is only a function of the upstream conditions, i.e. the incidence of the profile. The approximate solution of this real linear equations system is calculated using a Crout's factorisation method with partial pivoting.

The cavitation conditions are calculated using a method very similar to the one developed by Rowe & Lemonnier [2]. The cavity shape and the sigma value corresponding to its length are established

point are averaged over 10 batches of at least 512 samples. The variance of the mean estimate provides a way to check the quality of the results and to increase the batch number when the confidence interval does not meet the required accuracy.

In the Vx profiles in Figure 3-a, a velocity defect is apparent downstream of the main cavity closure. The Vy profiles in Figure 3-b indicate a strong deviation of the flow after the first station at 10% of the chord. This deviation propagates downstream to reach a vertical extension of 10 mm at the cavity closure, which does not exceed 2 mm in height, and is diffused up to the blade trailing edge. The strong variations of the profiles in Figure 3-a,b suggest that discrete structures are created from the first 10% of the blade and convected to the outer part of the flow with an inflexion in their trajectory at 45% of the chord. This is confirmed in Figure 3-c by the profiles given by the sum $(\overline{v_x'^2} + \overline{v_y'^2})$ of the velocity fluctuation autovariances. This sum represents the kinetic energy per unit mass of the large discrete structures, though the third component $\overline{v_z'^2}$ is missing. These structures have been observed by various authors in the wake of the main cavity. They have named them U-shaped or "Croissant" vortices [8], [9]. The local maxima of the kinetic energy profiles can be associated to the top of these inverse U-shaped discrete structures. The vertical extension of these structures grows rapidly above the main cavity, and is slowed down in the closure region. A strong increase in velocity fluctuations close to the wall seems to supply energy to the travelling discrete structures in this region of the flow.

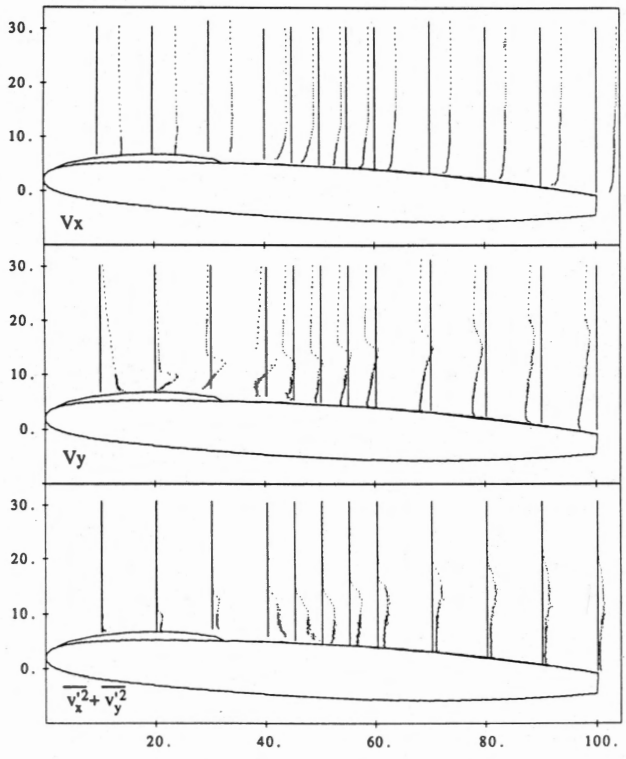

Figure 3 LDA measurements of the mean flow field over the NACA 009 blade suction side; i = 2.5°, σ =0.81, U_∞ = 20.7 m/s.
(a) Longitudinal component Vx of the mean velocity
(b) Transverse component Vy of the mean velocity
(c) Sum $\overline{v_x'^2} + \overline{v_y'^2}$ of the mean squared values of the components of the velocity fluctuations.

The signature of these coherent structures can be seen well because of the nature of the tracers used for the LDA measurements. The fact of using micro-bubbles for that purpose induced a slight deviation in the mean flow establishement. Due to low local pressure induced by the swirling structures, the micro-bubbles are not homogeously distributed in the fluid, but located around the latter. We therefore favoured the velocity measurement when these structures went through the measuring volume. If we compare the velocity profiles we have obtained to the only other measurements of such a type, to the best of our knowledge, presented by Kato in 1987 [9], one can observe that they are very close to the minimum of these latters in the longitudinal direction, and to their maximum in the normal direction. The similarity between the two studies is also remarkable if we look at the distribution of the rms velocity fluctuations.

This suggests that these inverse U-shaped discrete structures, inducing a negative velocity in the longitudinal direction and a positive velocity in the normal direction, are as well defined for small angles of incidence at high velocities as for large angles of incidence at low velocities. We can observe that these structures are generated at the blade leading edge and convected by the flow. In view of the results, we can ask if the distinction made between sheet cavitation and cloud cavitation is not only a matter of the intensity of these swirling structures.

Cavity shape measurements

The two-dimensional main cavity shape is determined by image processing. The cavity and the hydrofoil are illuminated with a laser sheet of light formed using a 5W Argon laser source, focused through a cylindrical lens with a focal length of 6 mm. The image of the reflected light on the cavity and on the hydrofoil surface is recorded with a 512x512 pixel CCD camera placed perpendicular to the test section window, with a small angle of inclination (See Figure 4).

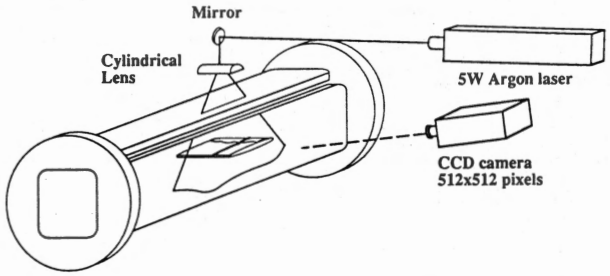

Figure 4 Schema of the optical mounting for cavity shape measurement by image processing.

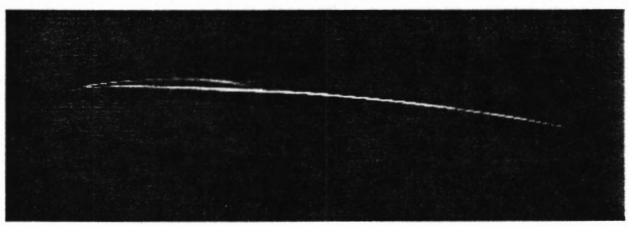

Figure 5 View of the reflected laser sheet on the cavity and on the hydrofoil.

For each operating point, two images are recorded. First of all, the image of the reflexion of the laser sheet of light on the hydrofoil without cavitation is recorded, to be used as a reference. Then, a

using an iterative method. The constant pressure constraint over the cavity can be translated into a constant tangential velocity value over the cavity :

$$v_t = U_\infty \sqrt{1+\sigma} \qquad (5)$$

Since the actual sigma value is unknown, an initial value is given for the first iteration. Elsewhere on the profile, the velocity is imposed as parallel to the wall, so v_n is equal to zero, except at three points in the wake of the cavity. The normal component of the velocity not being zero on the cavity at the first iteration, a joining law must be given in the wake of it. For that reason, a linear variation of the tangential velocity constraint to the normal velocity constraint on the three control points in its wake was chosen. This boundary condition is equivalent to a linear variation of the normal velocity component from a finite value on the cavity to a zero value on the wet part of the hydrofoil.

After each iteration, the control points on the cavity and in its wake are moved in the normal vector direction of a quantity proportional to the normal residual velocity component. This is expressed by the formula :

$$\Delta x_i = -C \cdot v_{n_i} \cdot \sin \alpha_i$$

$$\Delta y_i = -C \cdot v_{n_i} \cdot \cos \alpha_i \qquad (6)$$

where α_i is the profile slope at the control point, given by the slope of the same index panel. Points corresponding to the panel supports are then recalculated between two control points using a linear approximation. These points are slightly moved towards the inside of the profile to prevent any interference with it in the negative curvature areas.

Assuming the pressure coefficient at the trailing edge is not modified by the cavitating conditions, the preceding sigma value is corrected at each iteration step :

$$\sigma_i = \sigma_{i-1} + K \cdot \left(Cpr_{\text{without cavitation}} - Cpr_{i-1} \right) \qquad (7)$$

This sigma value adaptation is started only after the sixth iteration, in order to allow the cavity shape adjustment to be stabilised. The convergence, expressed by a normal velocity component on the cavity to be less than 1 % of the upstream velocity, is generally reached in about 15 to 20 iterations. As an example, the pressure coefficient distribution over the NACA profile at an incidence angle of 2.5 degrees and a cavity of 20 % of the chord length is given in Figure 7.

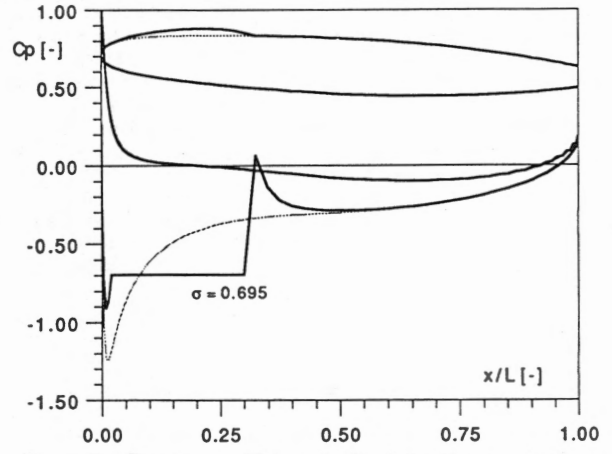

Figure 7 Pressure coefficient distribution without cavitation and for a cavity of 30% of the chord length given by a potential calculation.

In the same figure, we superimpose the cavity shape given by the calculation. The initial sigma value was 0.8 and converged pressure level on the cavity was -0.745.

Navier-Stokes code

We chose for that calculation a finite-element Navier-Stokes code called FIDAP [7]. A two-equation k-ε turbulent model and near-wall elements with specialized shape functions are used to do the calculation. To obtain a good convergence of the latter, a successive substitution algorithm (fixed point or Piccard iteration) with a relaxation scheme was chosen to solve the nonlinear terms. A weakened continuity formulation, called penalty function approach, given by :

$$\vec{\nabla} \cdot \vec{v} = \kappa \cdot p \qquad (8)$$

is applied instead of the classical continuity formulation to increase the convergence and to reduce the computation time. This method has been shown to be coherent if the penalty factor, κ, is set at a small enough value. In pratice, we performed the calculation with κ value of 10^{-6} and, after convergence, some additionnal iterations with a lower penalty value of 10^{-9} were done to increase the accuracy of the solution.

We used a non-dimensional formulation to solve the governing equations. The scaling units are the upstream velocity U_∞ and the hydrofoil chord length L. This scaling leads to :

a fluid density $\rho^* = 1$

a dynamic viscosity $\nu^* = 1/Re$,

a pressure $p^* = p/\rho U_\infty^2$

a turbulent kinetic energy $k^* = k/U_\infty^2$

and a turbulent dissipation $\varepsilon^* = \varepsilon L/U_\infty^3$

As regards the potential calculation, the upper and lower test section walls were taken into account in the calculation, as the development of the boundary layer on them has a large influence for the pressure distribution on the hydrofoil. The fluid elements used are 4-node quadrilateral elements on which the velocity components are approximated using bilinear interpolation functions. The pressure, calculated with a penalty formulation, is associated with the element centroïd. Boundary wall elements, as input and output elements are therefore 2-node linear elements. The mesh is generated using the preprocessor of the FIDAP package, called FIPREP. An unstructured H-mesh is chosen in order to obtain elements as perpendicular as possible to the hydrofoil and to the test section walls. Considerable refinement of the elements in the vicinity of the hydrofoil and of the test section walls is imposed to obtain wall elements of an order of magnitude corresponding to the viscous sublayer thickness. A refinement of the wall elements on the profile near the leading edge is also imposed to ensure a good geometric definition of this crucial region. Due to the truncated trailing edge, elements have been added in its wake, to help the code capturing the strong gradients in this region. The physical mesh of the test section and a closer view of the hydrofoil are presented in Figure 8.

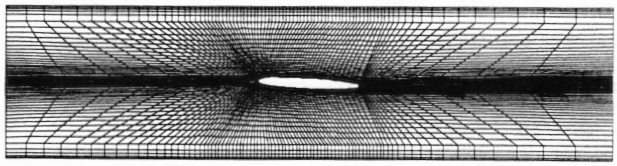

Figure 8 Physical mesh of the NACA 009 hydrofoil in the test section.

Boundary and initial conditions

The boundary conditions were deduced, as often as possible, from our measurement results. For the test section inlet, Dirichlet conditions are given for the velocity components, the turbulent kinetic energy and the dissipation. The degree of freedom restraints on the inlet boundary nodes are therefore a zero velocity component in the y direction and a unit velocity component in the x direction. A constant k^* value of 0.005, deduced from the measurement , and a constant estimated ε^* value of 0.05 are imposed.

On the test section outlet, Neuman conditions, i.e. zero fluxes, are given for all degrees of freedom. On the test section walls, as well as on the wet part of the hydrofoil, wall turbulent conditions are given, corresponding to a zero velocity on the wall elements and to special wall-law functions for the first near-wall elements. The k^* and ε^* values on the wall and the near-wall elements are automatically defined by the code using the local Reynolds number.

The initial conditions for the first iteration are given for the velocity components by the resolution of the linear Stokes equations. The initial k^* and ε^* values are everwhere equal to the inlet values. This first step is also used to verify the mesh generation.

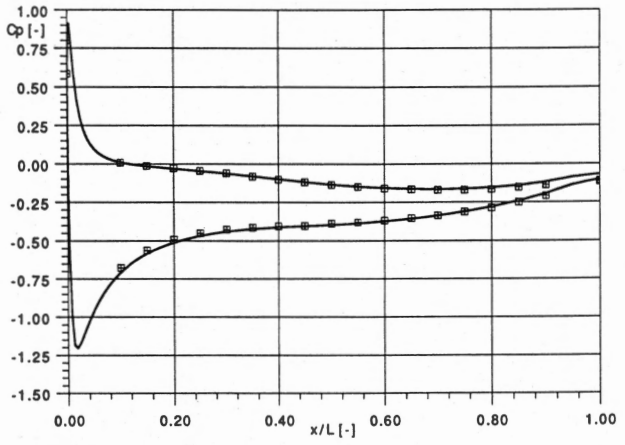

Figure 9 Comparison of the measured (#) and calculated (-) pressure coefficient distribution over a NACA 009 profile without cavitation for an angle of incidence of 2.5 degrees.

A result of the calculation for the non-cavitating situation on a NACA 009 hydrofoil with an angle of incidence of 2.5 degrees is compared in Figure 9 with the pressure measurements in the same conditions.

It can obviously be seen in this figure that the calculations agree very well with the experiments for the pressure distribution over the hydrofoil. This good result is confirmed by the hydrodynamic forces comparison which gives a difference between calculated and measured values of less then 1 % for the lift coefficient and less than 5 % for the drag coefficient.

For the cavitating situation, the problem is to define the boundary conditions to be imposed over the cavity. Looking at the measurements, despite the fact we cannot reach the exact position of the interface, we can observe that the velocity and Reynolds tensor components show a strong shear stress on the cavity surface, which seems to indicate that the interface plays the same role as a solid boundary. We thus impose on the cavity surface, as elsewhere on the hydrofoil surface, a solid wall condition. As roughly estimated as it seems to be, that boundary condition has the great advantage of being very simple and, following the measurement results, certainly more realistic than a slipping condition that we never observed.

Calculation results with cavitation

Applying the above boundary conditions to the geometry given by the potential result, we found a non-constant pressure value on the cavity (See Figure 10). This shows that neglecting the turbulent and viscous terms leads to underestimating the vertical expansion of the cavity and consequently to underestimating the sigma value for a given cavity length.

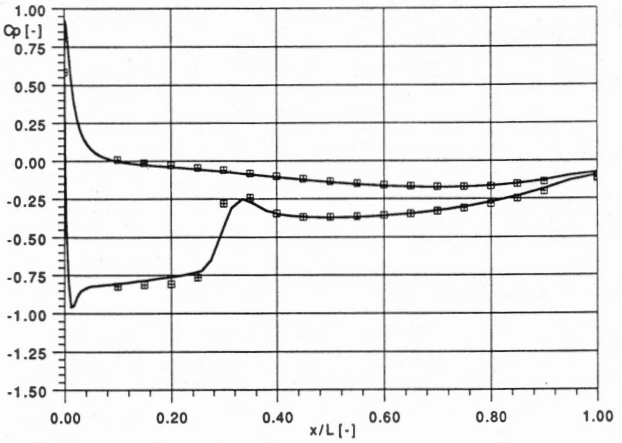

Figure 10 Result of the Navier-Stokes pressure coefficient distribution calculation on a cavity geometry given by a potential calculation.

Following the method described before, we reshape the cavity as a function of the pressure distribution given by this first Navier-Stokes result. The sole weakness of the method is the need for some trials to adapt the C deformation coefficient to obtain the flattest possible pressure distribution on the cavity. This was done after only two unsuccessful attempts. The final result is given in Figure 11.

COMPARISON OF CALCULATIONS AND EXPERIMENTS

The first result for comparison, because it is the most important in the erosion prediction, is the sigma value obtained for a given cavity length. We imposed for the potential calculation a relative cavity length x_c/L of 30 %. The resulting cavity end position, due to the point discretisation and cavity shape adaptation, was at a relative x_c/L value of 32 %. For such a cavity length and an upstream velocity of 20 m/s, the experimental sigma value is 0.81, based on the visualisations and the pressure measurements (see Figure 2). The potential calculation gives a sigma value of 0.745, and the Navier-Stokes correction gives a value of 0.80. Obviously, taking into account the dissipative terms leads to a much better estimation of the sigma value for a given cavity development. The prediction accuracy is better than 1.25 % for the Navier-Stokes result, instead of about 8 % for the potential case.

Comparing the two different calculated pressure coefficient distributions with the measured one for a sigma value of 0.81 and an upstream velocity of 20 m/s (see Figure 11) confirms these conclusions. The maximum recovery pressure positions are identical for the two results, but their levels are quite different : too large for the potential solution and too small for the Navier-Stokes one. The recovery pressure slopes are also different, much more similar to the measurements for the Navier-Stokes result. Finally, it can be observed that the Navier-Stokes calculation gives a much better

result than the potential solution at the trailing edge. This is due to a bad truncated trailing edge treatment in the potential code.

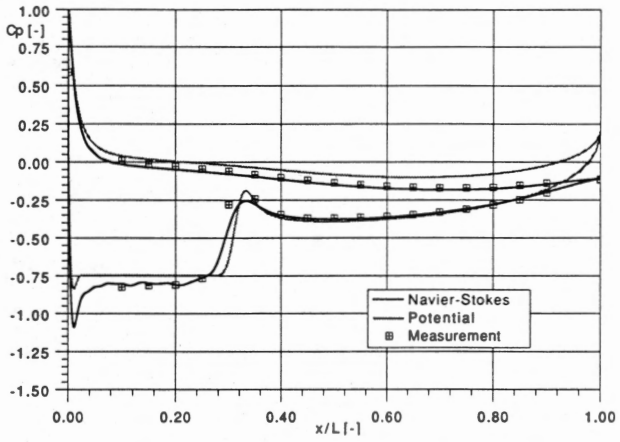

Figure 11 Comparison of the calculated pressure coefficient distributions with the measurements.

Cavity shape verification is another very informative comparison. This result gives a good idea of the physical validity of the calculation. Figure 12 compares the calculated cavity shapes with the results given by image processing. Only the suction side is presented and the vertical scale has been artificially enlarged in order to make the comparison easier. The symbols with an error bar are the measurements, and the two lines are the calculation results, the thinner cavity being the potential result.

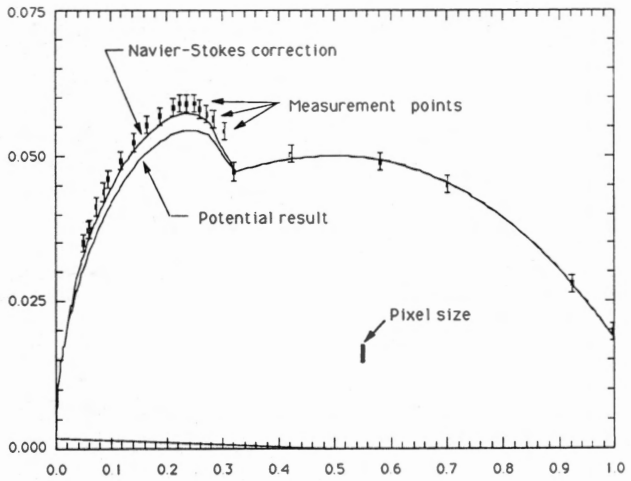

Figure 12 Cavity shape comparison between calculations (—) and measurements (⊞). Note the enlargement of the vertical scale.

The Navier-Stokes correction obviously tends to a more exact cavity shape. Though the latter calculated cavity elevation still seems to be slightly smaller then the measured one, it is inside of error bars everywhere but in the cavity closure. There, the measurement result gives a very abrupt closure far removed from the calculation result. This is because the cavity closure model used for the potential code, which the modification supplied by the Navier-Stokes code result cannot correct. This difference is of great importance and could explain the fact that the Navier-Stokes code was not able to capture the Reynolds influence. This result points out the need to find a better cavity closure model closer to the reality.

Another interesting aspect for the prediction of cavitation effects is the calculation of performance modifications due to cavity development. For an isolated hydrofoil, these performances are represented by the lift and drag forces. We have compared in Figure 13 the balance measurements with potential and Navier-Stokes code results with and without cavitation.

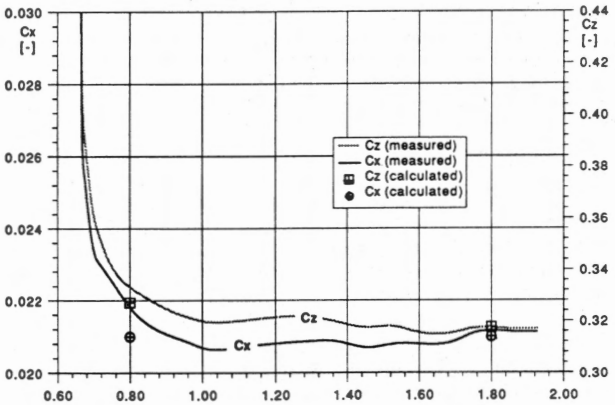

Figure 13 Measured and calculated lift and drag coefficients versus sigma value for a NACA 009 profile at an incidence angle of 2.5 degrees and an upstream velocity of 20 m/s.

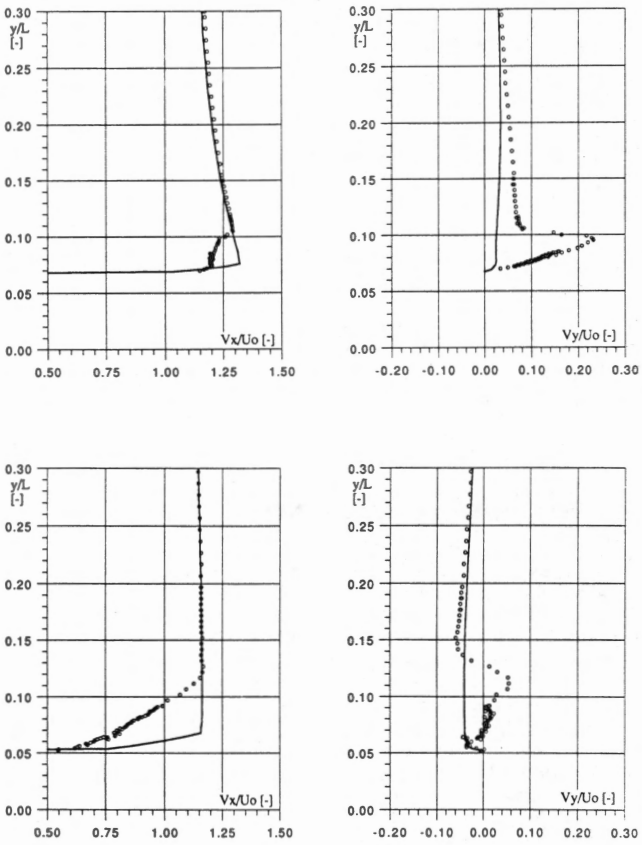

Figure 14 Comparison of measured and calculated transverse velocity profiles at (a) 20 % and (b) 45 % of the hydrofoil chord length.

On the one hand the Navier-Stokes result obtained for the lift coefficent prediction in the non-cavitating condition is good, but no better than the potential one. On the other hand, the lift increase with the appearance of cavitation is quite well followed by the Navier-Stokes calculation.

If the drag coefficient result is still excellent for the non-cavitating calculation, it fails to predict the drag increase with the cavity onset. This result is quite surprising. The drag of the cavity itself, modelised as a solid boundary, should increase the total drag of the hydrofoil. The cavity shape closure is certainly, once again, the reason for this surprising result. A gently sloping cavity closure does not increase the drag as a steep one would, due to the detachment thus induced.

The last measurements to compare with the calculation are the velocity components. Figures 14 (a) and (b) give the Navier-Stokes calculation and the LDA measurement results on vertical lines at 20 % (over the cavity) and 45 % (in its near wake) of the chord length.

The comparison is good except in a well-defined region, increasing in height in the flow direction, where a velocity default in the x direction and a positive y direction deviation occurs. As pointed out before, this deviation has been proved to be due, by comparison of the velocity results with visualisations, to discrete U-shaped vortices, generated at the leading edge cavity and convected by the flow, but it is overestimated due to the nature of the tracers used. Associating the difference between the measured and calculated results to the influence of these structures allows us to draw a diagram of their shape and their evolution in the flow direction presented in Figure 15.

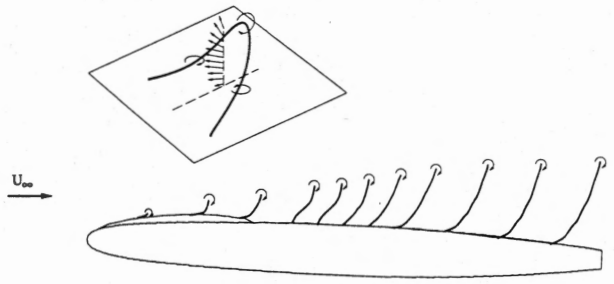

Figure 15 Sketch of the U-shaped vortex development based on the comparison between measured and calculated velocities.

CONCLUSIONS AND COMMENTS

The partial cavity on the leading edge of a NACA 009 hydrofoil has been successfully calculated using a method based on the use of both an indirect potential and a Navier-Stokes code. The cavity geometry given by the potential code is corrected with a Navier-Stokes computation on which the cavity surface is modelised as a solid boundary. If, with such a method, the erosion position can be well predicted for moderate Reynolds numbers up to $2 \cdot 10^6$, it fails to predict the Reynolds number influence for higher velocities as shown by our measurements. This lack of success and the comparison of the calculation results with the measurements call for two remarks. On the one hand, this result obviously proved that the cavity closure model used for the potential calculation needs to be improved. The unadapted model is the probable reason for the insensitiveness of the Navier-Stokes computation when increasing the Reynolds number. On the other hand, the comparison leads us to the conclusion that the unsteady discrete vorticity structures must be taken into account to reach an accurate prediction of the main cavity development. The influence of these structures on the mean flow certainly plays an increasing role for higher Reynolds numbers. Moreover, the calculation of these transient vortices, identified as erosive structures, is of major importance for erosion rate prediction. Our future aim is thus to be able to perform unsteady calculations in order to follow the evolution of these coherent structures. The only question is to determine how to modelise these strongly 3-D structures.

ACKNOWLEDGEMENTS

The authors wish to acknowledge the contribution made by all their colleagues from the IMHEF Cavitation Research Group. Thanks are also due to Mrs. Farhat and Kuhn de Chizelle, who performed the pressure measurements, and Mr. Gindroz for the balance measurements. This work is financially supported by the Swiss Federal "Commission d'Encouragement à la Recherche Scientifique", the Swiss energy producers association "Nationaler Energie Forschung Fonds", Sulzer Brothers and the Vevey Engineering Works.

BIBLIOGRAPHY

[1] **Lemonnier, H., Rowe, A.** (1988) : " *Another Approach in Modelling Cavitation Flows*", Journal of Fluid Mechanics, vol. 195, pp. 557+580, 1988

[2] **Ukon Y.** (1980) : " *Partial cavitation on two- and three-dimensional hydrofoils, and marine propellers.*", Proceedings of the 10th AIRH symposium, Tokyo, 1980, pp. 195-206

[3] **Favre, J.-N., Avellan, F., Ryhming, I.L.** (1987) : " *Cavitation Performance Improvement using a 2-D Inverse Method of Hydraulic Runner Design*", Proceedings of Int. Conf. on Inverse Design Concepts and Optimization in Engineering Science-II (ICIDES), October, 1987, Pennsylvania State University

[4] **Avellan F., Dupont, Ph., Ryhming, I.L.** (1988) : " *Generation Mechanism and Dynamics of Cavitation Vortices Downstream of a Fixed Leading Edge Cavity*", Proceedings of the 17th O.N.R. Symposium on Naval Hydrodynamics, 1988, The Hague, Netherlands

[5] **Delannoy, Y.** (1989) : " *Modélisation d'écoulements instationnaires et cavitants*", thèse, Institut National Polytechnique de Grenoble, France

[6] **Kubota A., Kato, H., Yamaguchi, H.** (1989) : " *Finite Difference Analysis of Unsteady Cavitation on a Two-Dimensionnal Hydrofoil*", Proceedings of the 5th Int. Conf. Numerical Ship Hydrodynamics, Sept. 1989, Hiroshima, Japan

[7] **Bercovier, M., Engelman, M.S.** (1979) : "*A Finite Element for Incompressible Fluid Flows*", J. Comp. Physics, vol. 30, 181, 1979

[8] **Van der Meulen, J.H.J** (1980) : "*Boundary Layer and Cavitation Studies of NACA 16-012 and NACA 4412 Hydrofoils*", 13th Symp. on Naval Hydrodynamics, Tokyo, 1980.

[9] **Kubota, S., Kato, H., Yamaguchi, H., Maeda, M.** (1987) : "*Unsteady Structure Measurement of Cloud Cavitation on a Foil Section Using Conditional Sampling Technique*", Proceedings of International Symposium on Cavitation Research Facilities and Techniques, ASME Winter Annual Meeting, Boston (USA), December 1987, Vol. 57, p. 161-168.

[10] **Avellan, F., Henry, P., Ryhming, I.L.** (1987) : "*A New High-Speed Tunnel for Cavitation Studies in Hydraulic Machinery.*", Proceedings of International Symposium on Cavitation Research Facilities and Techniques, ASME Winter Annual Meeting, Boston (USA), December 1987, Vol. 57, p. 49-60.

[11] **Wade, R.B., Acosta, A.J.** (1966) : " *Experimental Observations on the Flow Past a Plano-Convex Hydrofoil*", Trans. ASME, Ser. D, No. 88, pp. 273-283